1 **Ferruginous oceans during OAE1a and the collapse of the seawater**
2 **sulphate reservoir**
3
4
5 Kohen W. Bauer[1,2,‡], Cinzia Bottini[3], Sergei Katsev[4], Mark Jellinek[1], Roger
6 Francois[1], Elisabetta Erba[3], Sean A. Crowe[1,2, ‡*]
7
8 [1]Department of Earth, Ocean and Atmospheric Sciences,
9 The University of British Columbia, 2020 - 2207 Main Mall,
10 Vancouver, British Columbia V6T 1Z4, Canada
11
12 [2]Department of Microbiology and Immunology, Life Sciences Centre,
13 The University of British Columbia, 2350 Health Sciences Mall,
14 Vancouver, British Columbia, V6T 1Z3, Canada
15
16 [3]Department of Earth Sciences,
17 University of Milan, Via Mangiagalli 34,
18 20133 Milan, Italy
19
20 [4]Large Lakes Observatory and Department of Physics
21 University of Duluth, 2205 E 5th St,
22 Duluth, Minnesota, 55812, USA
23
24
25 *Corresponding author; sean.crowe@ubc.ca
26
27 ‡Current address; Department of Earth Sciences
28 University of Hong Kong
29 Pokfulam Road, Hong Kong SAR
30

31 At 28 mM seawater sulphate is one of the largest oxidant pools at Earth's

32 surface and its concentration in the oceans is generally assumed to have

33 remained above 5 mM since the early Phanerozoic (400 Ma). Intermittent

34 and potentially global oceanic anoxic events (OAEs) are accompanied by

35 changes in seawater sulphate concentrations and signal perturbations in

36 the Earth system associated with major climatic anomalies and biological

37 crises. Ferruginous (Fe-rich) ocean conditions developed transiently

38 during multiple OAEs, implying strong variability in seawater chemistry

39 and global biogeochemical cycles. The precise evolution of seawater

40 sulphate concentrations during OAEs remains uncertain and thus models

41 that aim to mechanistically link ocean anoxia to broad-scale disruptions in

42 the Earth system remain largely equivocal. Here we show that during

43 OAE1a, 125 Ma, the oceans were anoxic and ferruginous for more than 1

44 million years. Development of ferruginous conditions at this time requires

45 low seawater sulphate concentrations, which likely dropped to < 70 µM or

46 more than a hundred times lower than modern. This collapse in the

47 seawater sulphate pool over just a few hundred thousand years or less,

48 reveals previously unrecognized dynamics in Phanerozoic Earth surface

49 redox budgets with potential to dramatically alter global biogeochemical

50 cycles, marine biology, and climate on remarkably short time-scales.

51

52

53   Seawater chemistry is generally thought to have evolved to its current

54 well-oxygenated, sulphate-rich state between 540 and 420 million years ago (Ma)

55 [1, 2]. Throughout much of the preceding 3.5 billion years, the oceans were largely

56 anoxic, predominantly Fe-rich (ferruginous), and punctuated by intervals of

57 widespread hydrogen sulphide-rich conditions (euxinic) [3, 4]. These conditions

58 waned in the early Phanerozoic, and thus, for much of the last 500 Myr, marine

59 and global biogeochemical cycles were thought to have operated much as they

60 do today [5, 6]. Large-scale oceanic anoxic conditions, however, re-emerged

61 intermittently in the Phanerozoic Eon [7] and were particularly prevalent during

62 warm periods such as the Cretaceous. The oceans developed euxinia during a

63 number of these oceanic anoxic events (OAEs) [8, 9] when pelagic microbial

64 respiration was channelled through sulphate reduction producing hydrogen

65 sulphide that accumulated in poorly ventilated water masses. Emerging

66 evidence, however, also suggests that transient ferruginous conditions occurred

67 during several of the OAEs (OAE2, OAE3 and the end-Permian OAE) [8, 10, 11].

68 Since development of ferruginous conditions hinges on the balance between Fe

69 and S delivery and removal from the oceans [4], such temporal dynamics imply

70 large-scale variability in ocean chemistry and the S cycle.

71   Sulphur isotope signals and fluid inclusion data recorded during the

72 Cretaceous Period reveal that background seawater sulphate concentrations

73 were much lower (5 – 10 mM) [12, 13, 14, 15, 16] than the modern ocean (28 mM).

74 Episodic evaporite deposition likely drew down seawater sulphate concentrations

75 even further (possibly to as low as 1 mM), during the early Cretaceous [17]. This

76 evaporite deposition likely took place intermittently both before [18, 19], and after [20]

77 Aptian OAE1a (~125 Ma). Some stratigraphic reconstructions imply evaporite

78 deposition contemporaneous with OAE1a [21], however, this timing is not well

79 supported by independent chronostratigraphic data.

80   Low seawater sulphate concentrations could have strongly influenced

81 global biogeochemical cycling. For example, seawater sulphate concentrations

82 are an important control on marine methane (CH_4) cycling, with super-millimolar

83 sulphate concentrations attenuating the release of CH_4 generated in modern
84 marine sediments to the atmosphere through microbial anaerobic methane
85 oxidation [22, 23]. Sub-millimolar sulphate concentrations, in contrast, can lead to
86 large-scale oceanic CH_4 efflux with corresponding implications for climate [24].
87 While S-isotope data imply low mM sulphate concentrations [13, 14, 15, 17], existing
88 models and data lack the resolution needed to place robust upper limits on
89 possible marine sulphate concentrations that would facilitate reconstruction of the
90 climate system and the effects of OAE development on the biosphere.

91   To constrain seawater sulphate concentrations in the early Cretaceous,
92 we studied a suite of sedimentary rocks from the eastern margin of the Paleo-
93 Tethys Ocean (Cismon drill core) and the middle of the Paleo-Panthalassic
94 Ocean (Deep Sea Drilling Project (DSDP) Site 463) that capture OAE1a. This
95 interval is delineated by the deposition of organic matter (OM)-rich black shale
96 containing units for more than a million years [25, 26]. We analysed rocks from
97 OAE1a using selective sequential extractions to partition Fe speciation between
98 operationally defined phases (Supplementary Information), and distinguish
99 between Fe burial as pyrite and other forms of reactive Fe (i.e. non-lithogenic).
100 These sequential extractions target Fe-phases considered highly reactive (Fe_{HR} =
101 sum of all non-silicate Fe) towards sulphide (pyritization) and biological and
102 abiological Fe(III) reduction under anoxic conditions [27, 28, 29]. Fe-speciation
103 analyses thus enable us to discriminate between sediments deposited under
104 anoxic ferruginous versus euxinic water column states, based on the degree of
105 pyritization of this Fe_{HR} pool [4, 29]. Notably, preservation of Fe_{HR} in sediments that
106 also contain appreciable organic matter implies that pyritization was sulphate
107 limited [30].

108

109 **Ferruginous conditions during OAE1a**

110   OAE1a is characterized by a C-isotope excursion as well as by deposition
111 of OM-rich sediment, which are evident between ~18-24 m in the Cismon core
112 and ~615-625 m in DSDP Site 463 (Fig. 1). Our Fe-speciation analyses reveal

113 enrichments of pyritizable Fe (Fe_{HR}) across these same intervals in both Cismon

114 and DSDP Site 463 rocks (Fig. 1), relative to rocks stratigraphically above and

115 below. Ratios of Fe_{HR}/Fe_{Tot} >0.38 imply sediment deposition beneath anoxic

116 waters if ratios of Fe_{Tot}/Al are also >0.5 and C_{org} contents are >0.5 wt% [29, 31].

117 Fe_{HR}/Fe_{Tot} values recorded in the Cismon core during OAE1a are consistently

118 above 0.38 and indeed have Fe_{Tot}/Al >0.5 along with C_{org} >0.5 wt%, diagnostic of

119 deposition below an anoxic water column (Fig. 2). Fe_{HR}/Fe_{Tot} ratios in rocks that

120 bound OAE1a have Fe_{HR}/Fe_{Tot} <0.38) (Fig. 2). Fe_{HR}/Fe_{Tot} ratios in rocks

121 deposited at DSDP Site 463 also capture intervals with values >0.38 and Fe/Al

122 >0.5, similarly implying deposition under anoxic conditions. Some Fe_{HR}/Fe_{Tot}

123 values in sediments deposited during OAE1a at site 463, however, are below the

124 threshold (>0.38) used to diagnose anoxic ocean conditions and are thus

125 ambiguous to depositional redox state based on Fe-speciation alone. We note

126 however, that Fe-speciation analyses cannot diagnose sediment deposition

127 under oxic conditions. This is because of mass balance–under the current Fe-

128 speciation framework, enrichment of Fe_{HR} at one depositional location by

129 necessity requires its depletion in another. Ratios below 0.38 can thus also result

130 from deposition beneath an anoxic water column and instead likely signify a

131 remobilization of Fe_{HR} from such sites (Fig. 2). In strong contrast, continental

132 margin sediments, like those deposited at the Cismon site, likely served as the

133 main oceanic sinks for remobilized Fe_{HR}.

134   Fe_{Pyr}/Fe_{HR} ratios are a direct measure of the degree of pyritization of the

135 highly reactive Fe_{HR} pool and ratios >0.7 signal deposition under a euxinic water

136 column [27, 28, 32]. Values <0.7 indicate non-pyritized Fe_{HR} and, by definition, reveal

137 insufficient sulphide supply to pyritize the available Fe_{HR} thus precluding

138 accumulation of free sulphide and the development of euxinia. Values <0.7 in

139 sediments deposited under anoxic conditions (Fe_{HR}/Fe_{Tot} >0.38), signal sulphate

140 depletion and a ferruginous water column. All rocks deposited at the Cismon and

141 DSDP 463 sites during the OAE1a interval have Fe_{Pyr}/Fe_{HR} <<0.7 indicating

142 deposition under strictly non-euxinic, ferruginous conditions (Fig. 2).

143   As an additional test for depositional redox states we examined the

144   distribution of redox sensitive trace elements (RSTE) that can become enriched

145   under anoxic conditions [33, 34]. Sediments from both the Cismon and DSDP 463

146   sites are highly enriched in some RSTE throughout the OAE1a interval relative to

147   the post Archean average shale (PAAS) [35]. For example, rhenium (Re), an

148   element that is enriched under both ferruginous, and to a lesser degree euxinic

149   conditions, is highly enriched in OAE1a sediments, confirming deposition under

150   anoxic conditions at both sites (Fig. 2a, b). Deposition under euxinic conditions is

151   often accompanied by strong molybdenum (Mo) enrichment and euxinic

152   conditions can be conditionally inferred when sedimentary Mo concentrations are

153   greater than 25 µg g^{-1} [27]. Compilation of Mo concentrations in sediments

154   deposited across OAE1a [36, 37] shows that only 2 out of 162 samples analysed

155   have Mo concentrations greater than the 25 µg g^{-1} threshold (Fig. S8). This lack

156   of Mo enrichment, in light of Re enrichment, supports the Fe-speciation data,

157   which together show deposition under ferruginous rather than euxinic conditions.

158   Concentrations of Mo greater than 25 µg g^{-1} can be achieved through a variety of

159   processes [38], and in isolation, the two samples with greater than 25 µg g^{-1} need

160   not have been deposited under euxinic conditions. Instead, these rare Mo

161   enrichments likely reflect Fe-oxide and OM-Mo shuttling [39]. The general pattern

162   of strong RSTE enrichments (Cr, V, U, Re) with lack of corresponding Mo

163   enrichment in the OAE1a sediments, strongly contrasts observations from

164   modern euxinic sediments [33]. This can be seen when enrichment factors of these

165   RSTE are normalized to the ratio of the Mo enrichment factor in the OAE1a

166   sediments to the enrichment factors of Mo in example modern euxinic basins

167   (Fig. 2c, d). Most strikingly, Cr and Re are on average 350% and 2500% more

168   enriched in the Cismon sediments than in modern euxinic sediments, relative to

169   Mo, respectively (Fig. 2c, d). Based on the contrasting mechanisms that lead to

170   differential RSTE enrichments, our observations are best explained by deposition

171   of OAE1a sediments under strictly ferruginous and non-euxinic conditions.

172   Geochemical and petrographic information effectively rule out sample
173 storage artefacts, like oxidation of pyrite, and confirm that the conclusion for
174 deposition of OAE1a sediments under ferruginous conditions is robust. Prior work
175 suggests that sedimentary rocks can be subject to sample storage artefacts that
176 develop as a result of exposure to oxygen in the atmosphere and subsequent
177 oxidation of sedimentary pyrite [40, 41]. We consequently took care to work with
178 well-preserved rocks, but nevertheless also evaluated the extent to which post
179 depositional oxidation of Fe_{Pyr} in our samples could have led to false diagnosis of
180 either anoxic or ferruginous conditions (see Supplementary Information section
181 4). Oxidation converts pyrite and siderite to Fe-(oxyhydr)oxides and thus causes
182 redistribution of Fe from Fe_{Pyr} and Fe_{Carb} to Fe_{Ox}. Since these three pools are
183 summed in the Fe_{HR} pool, oxidation would not have impacted Fe_{HR}/Fe_{Tot} or Fe/Al
184 ratios, and thus could not have led to false diagnosis of anoxia based on Fe
185 speciation. Qualitatively, the preservation of both pristine framboidal pyrites (Fig.
186 S2) and abundant Fe_{Carb} (Table S4, S5) is inconsistent with pervasive post
187 depositional sample oxidation. Furthermore, we identify ferruginous conditions on
188 the basis of Fe_{Pyr}/Fe_{HR} <0.7, and since pyrite oxidation would decrease this ratio
189 it could lead to false diagnosis. We therefore tested the extent to which oxidation
190 might have altered Fe_{Pyr}/Fe_{HR} by summing Fe_{Ox}, the product of oxidation, and
191 Fe_{Pyr} to come up with a maximum possible pre-oxidation ratio, Fe'_{Pyr}/Fe_{HR}.
192 Fe'_{Pyr}/Fe_{HR} ratios in both the Cismon and DSDP site 463 sediments are mostly
193 below the conservative <0.7 threshold for the delineation of ferruginous
194 conditions (Fig. 2). This implies our conclusions are robust even in the unlikely
195 scenario where the entire Fe_{Ox} pool represents the product of pyrite oxidation.
196 Likewise, if total S (pyrite S and any S pool resulting from oxidation) is used as a
197 proxy for pre-oxidation pyrite (Fe''_{Pyr}), Fe''_{Pyr}/Fe_{HR} also remain mostly below the
198 0.7 threshold (Fig. S2). We also note, that our RSTE data would be unaffected by
199 sample oxidation. Collectively, therefore, our Fe speciation and RSTE data
200 unambiguously document deposition of both DSDP and Cismon sediments under
201 ferruginous conditions.

202

Aptian seawater sulphate concentrations

To constrain Aptian seawater sulphate concentrations, we constructed a 1D water-column reactive transport model (see Supplementary Information) to simulate complete sulphate drawdown through microbial sulphate reduction that would permit the development of ferruginous conditions in a stratified Cretaceous ocean. Pyrite burial fluxes calculated by combining sedimentation rates [26] with sediment pyrite concentrations tether our 1D water column model outputs to the geologic record and place upper limits on the flux of sulphate that can be converted to pyrite through microbial sulphate reduction and reaction of the sulphide produced with Fe_{HR}, either directly in the water column or in bottom sediments (see Supplementary Information section 6). With microbial sulphate reduction rates parameterized based on modern marine ecosystems and analogies to low-sulphate ferruginous environments [42, 43] our water column modelling yields an average estimate for seawater sulphate of 5-10 µM, but not more than 70 µM (Fig. 3). Similar results are obtained modelling sulphate reduction rates in underlying sediments (Table S8). We note that the low sulphate reduction rates in our models are also consistent with the large S-isotope fractionations observed in Cismon pyrites and pyrites deposited elsewhere during OAE1a [15], given that large S-isotope fractionations tend to develop at low sulphate reduction rates [44]. The large S-isotope fractionations recorded in the Cismon pyrites, however, may also require a contribution from S disproportionation ($\delta^{34}S_{pyrite} \approx$ -47‰ [13], Fig. S4) which is known to be active in modern Fe-rich sediments [45]. Imposing higher sulphate concentrations in our models with realistic rates of sulphate reduction, sedimentation rates, and transport across oceanic pycnoclines or the sediment-water interface, yield pyrite burial fluxes much higher than those recorded in Cismon rocks. Alternatively, these lead to residual sulphate in deep waters and are thus incompatible with the Fe speciation data and ferruginous depositional conditions (Fig 3). Our results

231   thus constrain seawater sulphate concentrations during OAE1a, to more than a

232   hundred times lower than the modern.

233   Our observation of ferruginous conditions during OAE1a require a decline

234   of the seawater sulphate pool from low mM to µM concentrations in a time frame

235   of less than 100 kyr, commensurate with the initiation of OAE1a, as delineated by

236   the carbon isotope record. Previous studies suggest that seawater sulphate

237   concentrations were drawn down to as low as 1 mM over millions of years

238   preceding OAE1a as the result of evaporite deposition associated with the

239   opening of the South Atlantic [17]. Evaporite mineral deposition effectively draws

240   sulphate down from modern day concentrations of 28 mM to 1 mM, but when

241   sulphate concentrations drop below 1 mM, seawater saturation with respect to

242   sulphate-minerals (gypsum) during evaporation requires unrealistically high Ca^{2+}

243   concentrations that are inconsistent with reconstructions for Aptian seawater

244   chemistry [12, 46] (see Supplementary Information). Our observation of ferruginous

245   conditions and sub-mM seawater sulphate concentrations thus effectively rules

246   out contemporaneous deposition of black shale and gypsum in evaporites during

247   the OAE1a interval itself. This instead implies that evaporite deposition took

248   place before OAE1a, in the Late Barremian to early Aptian as previously

249   considered [21]. Seawater sulphate drawdown to µM concentrations therefore

250   requires a second phase of sulphate sequestration and alternative burial

251   mechanisms. Another important sink for seawater sulphate is microbial sulphate

252   reduction and pyrite deposition and burial. Expansion of this sink during OAE1a

253   provides a plausible mechanism to lower seawater sulphate to µM

254   concentrations and drive development of ferruginous conditions, which we

255   explore below.

256   Enhanced pyrite burial associated with the expansion of ocean anoxia

257   helps balance strong hydrothermal and weathering inputs of S to the oceans

258   during OAE1a. Coupled models of strontium and sulphur isotopes provide

259   compelling evidence for enhanced hydrothermalism and continental weathering

260   at this time [14, 15]. The development of ferruginous conditions as well as S budgets

261   and S isotope mass balances (see Supplementary Information), however, require

262   additional sinks for marine sulphate that balance these enhanced S inputs.

263   Sulphur mass balance modelling reveals that an increase in global pyrite

264   deposition rates from 0.66 to a maximum of 2.9 Tmol yr^{-1} (Fig 4a), offsets some

265   of the enhanced S inputs while remaining consistent with the isotope record (Fig.

266   4b). We note that pyrite deposition rates are higher under anoxic water columns

267   [47] and thus the increase in pyrite burial could be achieved by expanding the

268   global extent of water column anoxia. For example, if water column anoxia

269   expanded from 0.1%, its extent in the modern ocean [48], to between 2 and 10%,

270   the increase from 0.66 to 2.9 Tmol yr^{-1} could be achieved with area specific pyrite

271   deposition rates between 0.08 and 0.4 mol S m^{-2} yr^{-1} in regions of ocean anoxia,

272   which is similar to rates of pyrite burial in sediments underlying modern OMZs [49,

273   50] (Fig. 4a and Supplementary Information Fig. S6). This pyrite burial interval

274   would also drive an increase in the δ^{34}S composition of seawater sulphate due to

275   enhanced burial of isotopically light S in pyrite. Such an increase in seawater

276   sulphate δ^{34}S appears to be recorded in some carbonate associated sulphate

277   (CAS), providing geological evidence for such pyrite burial (Fig 4c) [14, 15]. Mass

278   balance using this same S isotope data constrains maximum pyrite depositional

279   rates to not much more than 2.9 Tmol yr^{-1}, yet given the strong input fluxes from

280   hydrothermalism and weathering another S sink is needed to draw seawater

281   sulphate concentrations down to levels that support ferruginous conditions.

282   Biomass associated organic S is an additional, yet often overlooked,

283   sulphur sink that when combined with pyrite burial, is sufficiently large to draw

284   seawater sulphate down to µM concentrations. S-isotope mass balance requires

285   that this additional sink carries near seawater δ^{34}S values. Sinks such as

286   biomass derived organic S, CAS, or barite associated with organic matter, are all

287   known to operate in low sulphate modern and ancient environments [51, 52]. While

288   biomass associated organic S has been shown to be a major pathway for S

289   burial in lacustrine environments [53, 54], it is often neglected in the marine S cycle.

290   Marine organisms are characterized by C:S molar ratios of 50:1 [55, 56, 57], and thus

291   the burial flux of organic S is likely on the order of 5 wt% that of organic C. Note

292   that this biomass associated organic S is distinct from S added to OM during

293   diagenesis (i.e., through sulphurization reactions [58]). Given the total S and

294   organic matter contents of the Cismon sediments deposited during OAE1a [59],

295   and assuming all non-pyrite S is buried as biomass associated organic S, we

296   calculate an average OM C:S molar ratio of ~45, revealing that OM buried during

297   OAE1a has a similar C:S composition to that of modern biomass [57]. This

298   supports the idea that during intervals of increased OM burial, biomass

299   associated organic S is an important sink from the ocean. Marine organisms,

300   furthermore, assimilate S with a $\delta^{34}S$ composition nearly identical to seawater [56,

301   60, 61]. Given pre-OAE1a primary production similar to modern (48 Gt C yr^{-1}) [48] and

302   OM that is ~5 wt% S, the dramatic (up to a 35-fold [59]) increase in OM burial

303   during OAE1a would be, together with pyrite burial, more than sufficient (up to

304   7.5 Tmol yr^{-1}) to remove most of the S entering the ocean at this time (5.3 Tmol

305   yr^{-1}). Development of ferruginous conditions can thus be attributed to widespread

306   anoxia and ensuing pelagic sulphate reduction and enhanced burial of biomass

307   associated organic S against the backdrop of low Cretaceous seawater sulphate

308   concentrations as well as strong hydrothermalism and weathering. Following

309   OAE1a, the seawater sulphate pool can rebound to mM sulphate concentrations

310   in less than 2 Myr (Fig 4b), allowing for evaporite deposition as early as ~122 Ma,

311   a timing also consistent with known post OAE1a evaporite stratigraphies [20].

312

313   **Implications**

314   At 28 mM, seawater sulphate is an oxidant pool twice the size of modern

315   atmospheric O_2. A decline to low µM seawater sulphate concentrations thus

316   indicates a reorganization of global oxidant pools during OAE1a with implications

317   for marine ecology, biogeochemical cycling, and climate. Water column anoxia,

318   for example, may have extended at least transiently into the photic zone during

319   OAE1a with potential to influence photosynthetic ecology. Biomarkers indicative

320   of green S bacteria have indeed been recovered in sediments deposited during

321 OAE1a [62, 63]. While green S bacteria are best known as sulphide oxidizing

322 phototrophs [64], they are also known to grow on ferrous Fe (photoferrotrophy) and

323 were likely key primary producers in the ferruginous oceans of the Precambrian

324 [65]. Preservation of biomarkers from green S bacteria in Aptian ferruginous

325 sediments may thus signal the return of photoferrotrophy to the Phanerozoic

326 oceans. At the same time, low-sulphate, ferruginous ocean conditions would

327 have both channelled organic matter degradation from sulphate reduction to

328 methanogenesis and precluded the consumption of this methane through

329 anaerobic oxidation with sulphate. Earth system modelling indeed shows that

330 seawater sulphate concentrations below 1 mM promote massive marine methane

331 fluxes to the atmosphere with attendant greenhouse warming [24].

332   Development of ferruginous conditions during OAE1a thus reveals large-

333 scale dynamics in Earth's biogeochemical cycles over intervals of less than a

334 hundred thousand years (Fig. 4). The development of ferruginous ocean

335 conditions during multiple OAEs [8, 11] may thus signify a general instability in Earth

336 surface redox budgets and the recurrent reorganization of major oxidant pools at

337 Earth's surface, like seawater sulphate, during the Phanerozoic Eon. The

338 mechanisms driving this reorganization remain uncertain, but could be addressed

339 through better constraints on global S budgets and the drivers of ocean de-

340 oxygenation, as well as the development of Earth system models that resolve

341 such large-scale biogeochemical dynamics over relatively short time scales.

342
343
344
345
346
347
348
349
350
351
352
353
354

Figure Captions

Figure 1. Fe-speciation and carbon isotope records for Cismon and DSDP Site 463. Integrated stratigraphy of the Cismon and DSDP Site 463 after [25, 66]. The grey shaded region (OAE1a) represents ~1.1 Mya [26], C-isotope stages C2–C7 [14, 26, 67]. Panels (a-e) are Cismon data and panels (f-j) are DSDP Site 463 data (**a**) Cismon carbon isotope data from [66]. Rhenium concentration data from [59]. (**b**) Carbonate C after [68], and organic matter C data after [59]. (**c**) $Fe_{Pyritizable}$; sum of all pyritizable Fe_{HR} pools (Fe_{Carb}, Fe_{OM}, Fe_{Ox}) (**d**) Fe_{Sil}; silicate Fe (**e**) Fe_{Pyr}; pyrite Fe. Green diamonds represent pyrite concentration data from [13]. (**f**) DSDP Site 463 carbon isotope data from [59]. Rhenium concentration data from [59]. (**g**) Carbonate C data from [66], organic C data from [63, 66]. (**h**) $Fe_{Pyritizable}$; sum of all pyritizable Fe_{HR} pools (Fe_{Carb}, Fe_{OM}, Fe_{Ox}) (**i**) Fe_{Sil}; silicate Fe. (**j**) Fe_{Pyr}; pyrite Fe. The start of the nannoconid decline and beginning of the nannoconid crisis are marked with dashed lines [25].

Figure 2. (**a**) Fe-speciation and Fe/Al records of the Cismon and DSDP Site 463 (**b**). The vertical and horizontal dotted lines refer to the oxic-anoxic threshold ($Fe_{HR}/Fe_{Tot} = 0.38$) and a conservative ferruginous-euxinic threshold ($Fe_{Pyr}/Fe_{HR} = 0.70$) respectively. The open circles represent Fe'_{Pyr}/Fe_{HR}, the maximum possible amount of pyrite present in the samples assuming the very unlikely scenario where the entire Fe_{Ox} pool is a result of pyrite oxidation. The solid vertical line in the top panels refers to the Fe/Al ratio of 0.5. The solid vertical line in the bottom panels refers to the average rhenium concentration of the PAAS, with the purple shading representing a 2 sigma uncertainty on this value (0.4 pbb, [69]). Litho-, bio- and magneto-stratigraphy is the same as for Figure 1. OAE1a redox sensitive trace element (RSTE) enrichment factors for the Cismon core (**c**) and DSDP site 463 (**d**) compared to modern euxinic sediments. Displayed are enrichment factors of RSTE normalized to the ratio of the Mo enrichment factor in the OAE1a sediments to the enrichment factors of Mo in example modern euxinic basins, Cariaco Basin and Saanich Inlet sediments. We find that the RSTE enrichment factors of Cr and Re, metals that do not require free sulphide to be buried under anoxic conditions, are dramatically enriched in both the Cismon and DSDP 463 sediments, relative to modern euxinic basins.

Figure 3. Models of marine S cycling during OAE1a. (**a**) Modelled rates of microbial sulphate reduction in a stratified ocean water column with different surface seawater sulphate concentrations. The upper 100 m represents the surface mixed layer, which we assume is well oxygenated. (**b**) Resulting sulphate concentration profiles. (**c**) Water column depth integrated sulphate reduction rates (pyrite burial). The parameter space represents modelled depth integrated sulphate reduction rates consistent with complete water column sulphate drawdown, as a function of initial seawater sulphate concentration and the maximum rate of sulphate reduction (V_{max}). To conservatively allow for uncertainties in the sedimentation rate at the Cismon site, we scaled up the average pyrite depositional flux determined for the Cismon sediments by two factors; 7.8 ($C_{Pyr}^{7.8}$) to allow for the possibility of higher sedimentation rates like those observed in modern environments like the Peru Margin and Black Sea, and 25 (C_{Pyr}^{25}), to allow for even higher sedimentation rates like those observed in the modern Cariaco Basin. Such higher sedimentation rates would lead to higher pyrite burial fluxes in the Cismon and DSDP site 463 sediments, and would support higher upper estimates on the flux of

403 sulphate that can be converted to pyrite through microbial sulphate reduction. The pink
404 box outlines the solution space corresponding to the average pyrite depositional flux
405 observed in the Cismon sediments (350 μmol m^{-2} yr^{-1}), including the upper estimate
406 produced by the scaling factor ($C_{Pyr}^{7.8}$), whereas the green box solution space outlines
407 the range of pyrite depositional fluxes observed at the Cismon site scaled for even
408 higher sedimentation rates (C_{Pyr}^{25}). We note that imposing higher rates of water column
409 sulphate reduction in our model leads to pyrite deposition rates much higher than those
410 recorded in the Cismon and DSDP site 463 sediments during OAE1a.

411
412 Figure 4. Evolution of the Cretaceous seawater sulphate reservoir. The coloured bars
413 represent the conceptual model and proposed timing of early Cretaceous events
414 associated with the development of OAE1a [13, 20, 21, 59]. (**a**) Modelled S input and burial
415 fluxes. The blue line represents hydrothermal and weathering S input after [14, 15]. The
416 black line is our modelled pyrite burial flux. The pink line represents the burial of S in
417 evaporites and the green line represents a non-fractionated sink of S needed to account
418 for total S burial during OAE1a. (**b**) The blue line is our model result for the evolution of
419 seawater sulphate concentrations. The green shading represents the relative timing of
420 OAE1a. (**c**) Isotopic composition of Aptian seawater sulphate. The blue line represents
421 our model results for the evolution of $\delta^{34}S_{sulphate}$. The grey data points represent
422 $\delta^{34}S_{sulphate}$ data from [14]; squares, [15]; diamonds, [70]; crosses and [13]; triangles. The diamond
423 distribution plot at the right is a compilation of this sedimentary $\delta^{34}S_{Sulphate}$ data with the
424 grey shading delineating the 5th and 95th percentiles, encompassing 90% of the early
425 Aptian $\delta^{34}S_{Sulphate}$ data.

426
427

437
438 **Data availability statement**

439
440 The datasets and models generated during and/or analysed during the current
441 study are available from the corresponding author on reasonable request.
442
443
444
445
446
447
448

449 1.   Kump LR, Brantley SL, Arthur MA. Chemical, weathering, atmospheric CO2,
450   and climate. *Annual Review of Earth and Planetary Sciences* 2000, **28:** 611-
451   667.
452
453 2.   Stolper DA, Keller CB. A record of deep-ocean dissolved O2 from the
454   oxidation state of iron in submarine basalts. *Nature* 2018, **553**(7688)**:** 323-
455   327.
456
457 3.   Planavsky NJ, Reinhard CT, Wang X, Thomson D, McGoldrick P, Rainbird RH*,
458   et al.* Low Mid-Proterozoic atmospheric oxygen levels and the delayed rise of
459   animals. *Science* 2014, **346**(6209)**:** 635-638.
460
461 4.   Poulton SW, Canfield DE. Ferruginous Conditions: A Dominant Feature of the
462   Ocean through Earth's History. *Elements* 2011, **7**(2)**:** 107-112.
463
464 5.   Berner RA, Canfield DE. A new model for atmospheric oxygen over
465   Phanerozoic time. *American Journal of Science* 1989, **289**(4)**:** 333-361.
466
467 6.   Bergman NM, Lenton TM, Watson AJ. COPSE: A new model of biogeochemical
468   cycling over Phanerozoic time. *American Journal of Science* 2004, **304**(5)**:**
469   397-437.
470
471 7.   Jenkyns HC. Geochemistry of oceanic anoxic events. *Geochemistry Geophysics
472   Geosystems* 2010, **11:** 30.
473
474 8.   Poulton SW, Henkel S, Marz C, Urquhart H, Flogel S, Kasten S*, et al.* A
475   continental-weathering control on orbitally driven redox-nutrient cycling
476   during Cretaceous Oceanic Anoxic Event 2. *Geology* 2015, **43**(11)**:** 963-966.
477
478 9.   Kuypers MMM, Pancost RD, Nijenhuis IA, Damste JSS. Enhanced productivity
479   led to increased organic carbon burial in the euxinic North Atlantic basin
480   during the late Cenomanian oceanic anoxic event. *Paleoceanography* 2002,
481   **17**(4).
482
483 10.   Marz C, Poulton SW, Beckmann B, Kuster K, Wagner T, Kasten S. Redox
484   sensitivity of P cycling during marine black shale formation: Dynamics of
485   sulfidic and anoxic, non-sulfidic bottom waters. *Geochimica Et Cosmochimica
486   Acta* 2008, **72**(15)**:** 3703-3717.
487
488 11.   Clarkson MO, Wood RA, Poulton SW, Richoz S, Newton RJ, Kasemann SA*, et al.*
489   Dynamic anoxic ferruginous conditions during the end-Permian mass
490   extinction and recovery. *Nature Communications* 2016, **7**.
491
492 12.   Timofeeff MN, Lowenstein TK, da Silva MA, Harris NB. Secular variation in
493   the major-ion chemistry of seawater: Evidence from fluid inclusions in
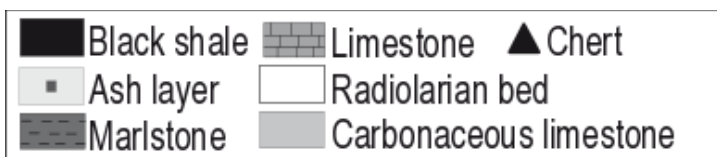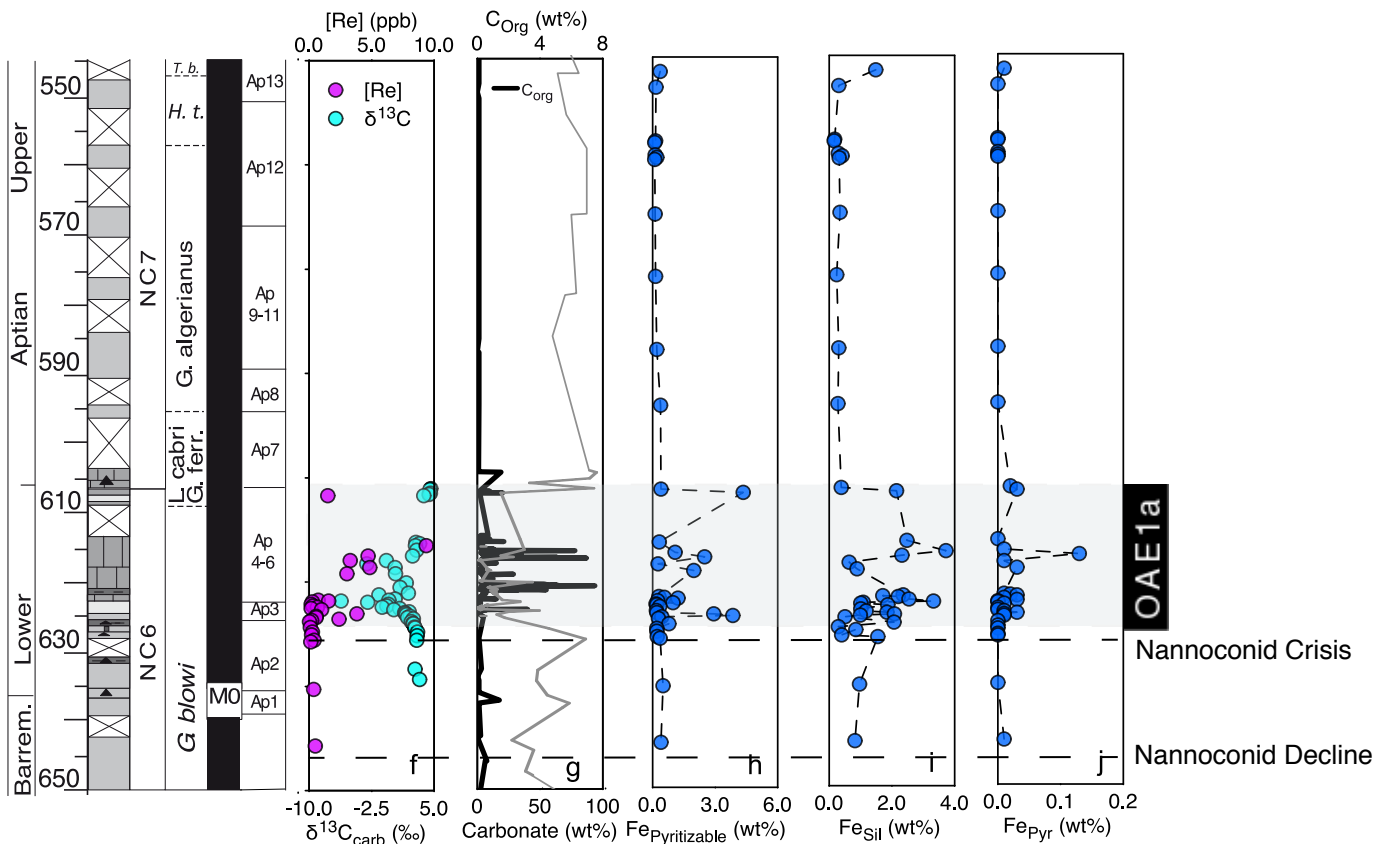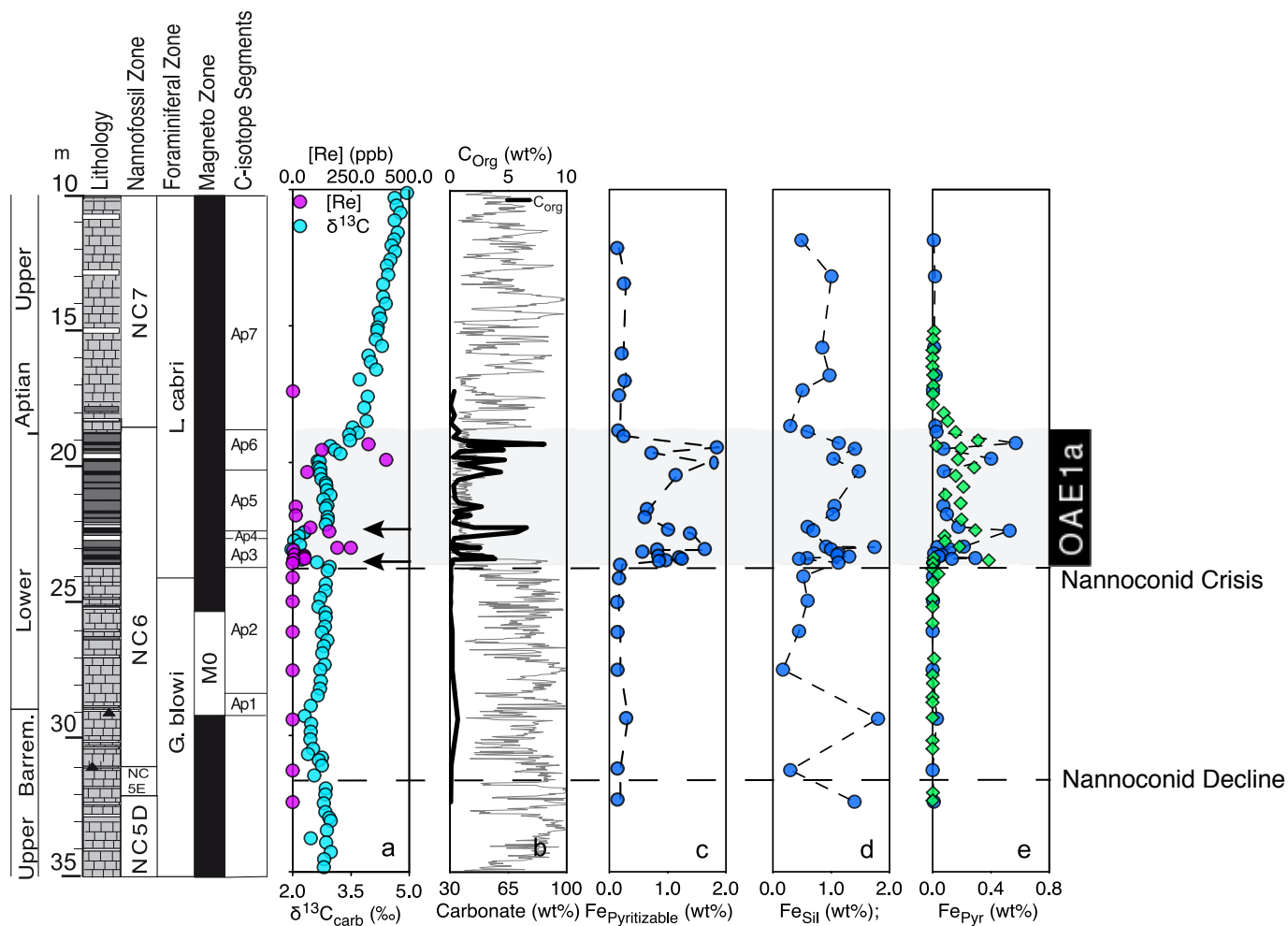494   Cretaceous halites. *Geochimica Et Cosmochimica Acta* 2006, **70**(8).

495

496 13. Gomes ML, Hurtgen MT, Sageman BB. Biogeochemical sulfur cycling during
497 Cretaceous oceanic anoxic events: A comparison of OAE1a and OAE2.
498 *Paleoceanography* 2016, **31**(2)**:** 233-251.

499

500 14. Mills JV, Gomes ML, Kristall B, Sageman BB, Jacobson AD, Hurtgen MT.
501 Massive volcanism, evaporite deposition, and the chemical evolution of the
502 Early Cretaceous ocean. *Geology* 2017, **45**(5)**:** 475-478.

503

504 15. Kristall B, Jacobson AD, Sageman BB, Hurtgen MT. Coupled strontium-sulfur
505 cycle modeling and the Early Cretaceous sulfur isotope record.
506 *Palaeogeography Palaeoclimatology Palaeoecology* 2018, **496:** 305-322.

507

508 16. Lowenstein TK, Hardie LA, Timofeeff MN, Demicco RV. Secular variation in
509 seawater chemistry and the origin of calcium chloride basinal brines. *Geology*
510 2003, **31**(10)**:** 857-860.

511

512 17. Wortmann UG, Chernyavsky BM. Effect of evaporite deposition on Early
513 Cretaceous carbon and sulphur cycling. *Nature* 2007, **446**(7136)**:** 654-656.

514

515 18. Davison I. Geology and tectonics of the South Atlantic Brazilian salt basins.
516 *Geological Society, London, Special Publications* 2007, **272**(1)**:** 345-359.

517

518 19. Bate RH. Non-marine ostracod assemblages of the Pre-Salt rift basins of West
519 Africa and their role in sequence stratigraphy. *Geological Society, London,*
520 *Special Publications* 1999, **153**(1)**:** 283-292.

521

522 20. Chaboureau AC, Guillocheau F, Robin C, Rohais S, Moulin M, Aslanian D.
523 Paleogeographic evolution of the central segment of the South Atlantic
524 during Early Cretaceous times: Paleotopographic and geodynamic
525 implications. *Tectonophysics* 2013, **604:** 191-223.

526

527 21. Tedeschi LR, Jenkyns HC, Robinson SA, Sanjines AES, Viviers MC, Quintaes C*,*
528 *et al.* New age constraints on Aptian evaporites and carbonates from the
529 South Atlantic: Implications for Oceanic Anoxic Event 1a. *Geology* 2017,
530 **45**(6)**:** 543-546.

531

532 22. Knittel K, Boetius A. Anaerobic Oxidation of Methane: Progress with an
533 Unknown Process. *Annual Review of Microbiology* 2009, **63:** 311-334.

534

535 23. Reeburgh WS. Oceanic methane biogeochemistry. *Chemical Reviews* 2007,
536 **107**(2)**:** 486-513.

537

538 24. Olson SL, Reinhard CT, Lyons TW. Limited role for methane in the mid-
539 Proterozoic greenhouse. *Proceedings of the National Academy of Sciences of*
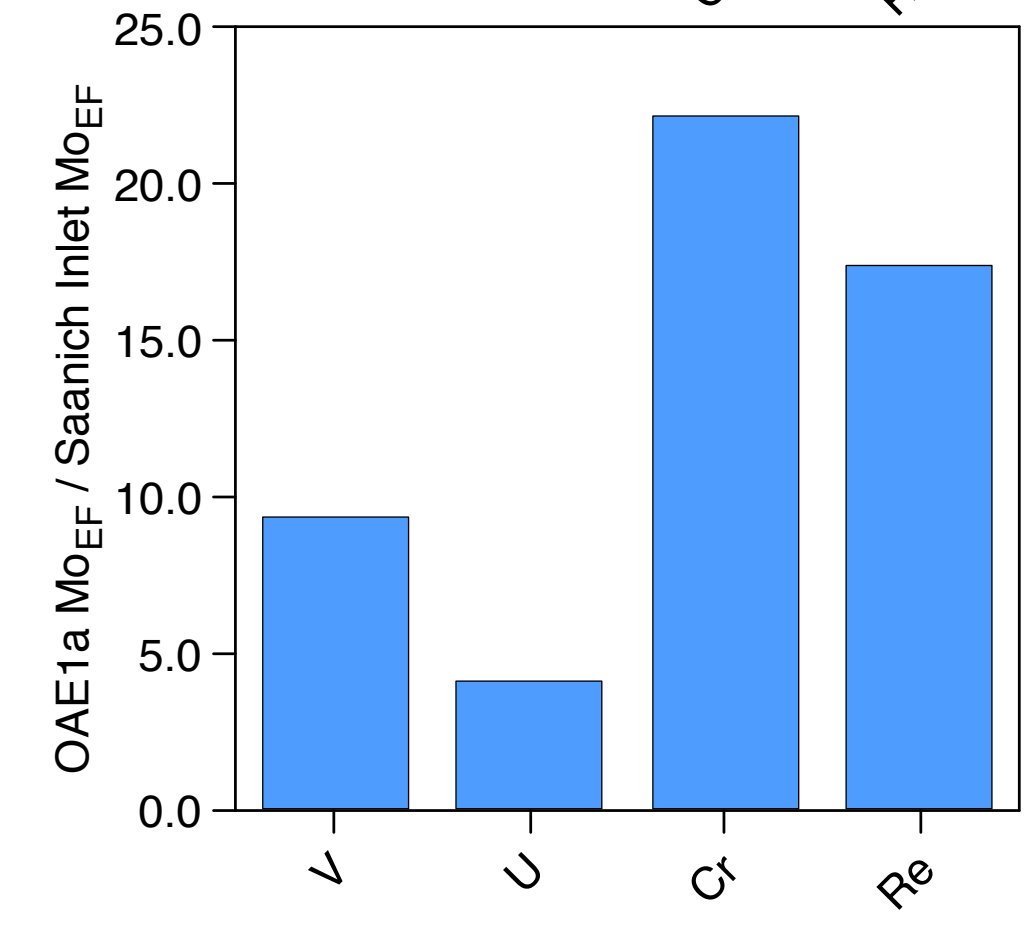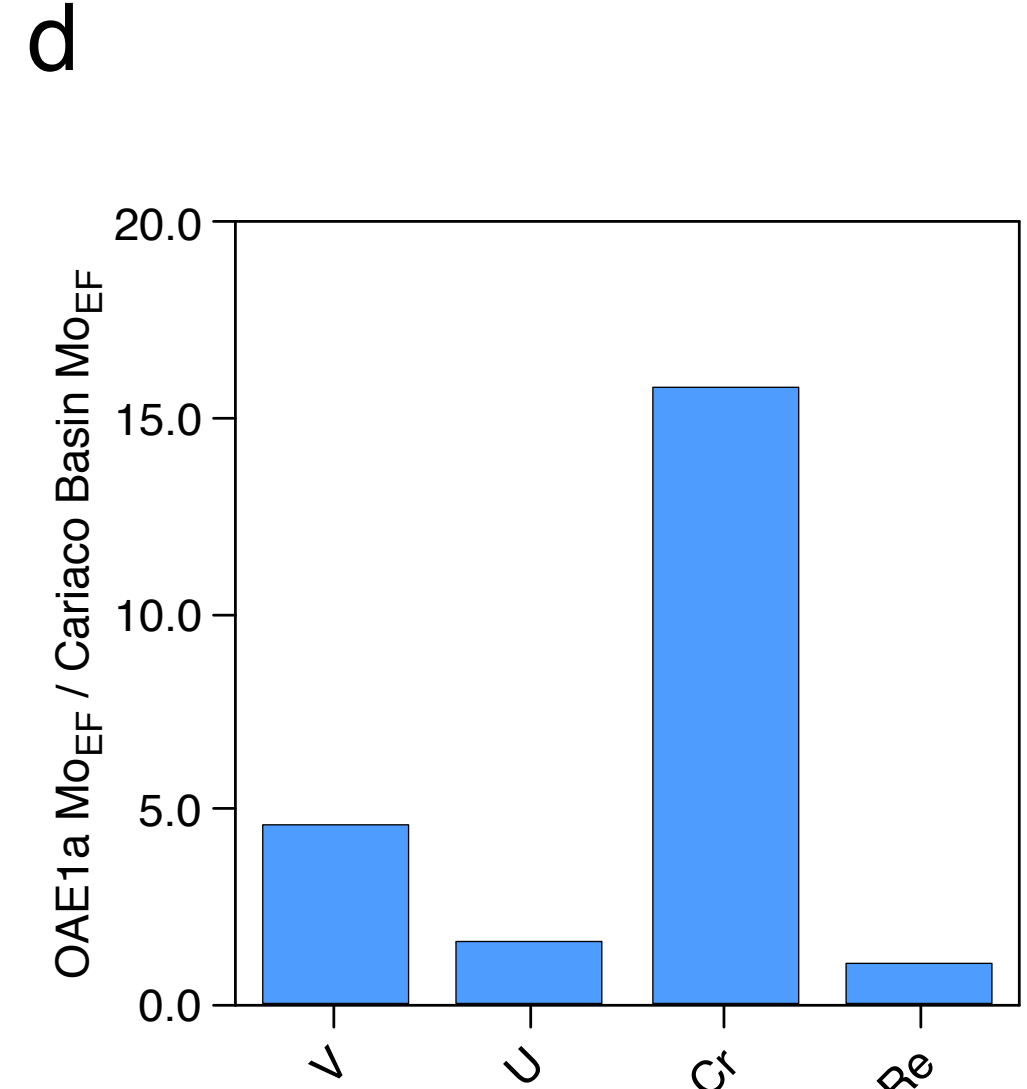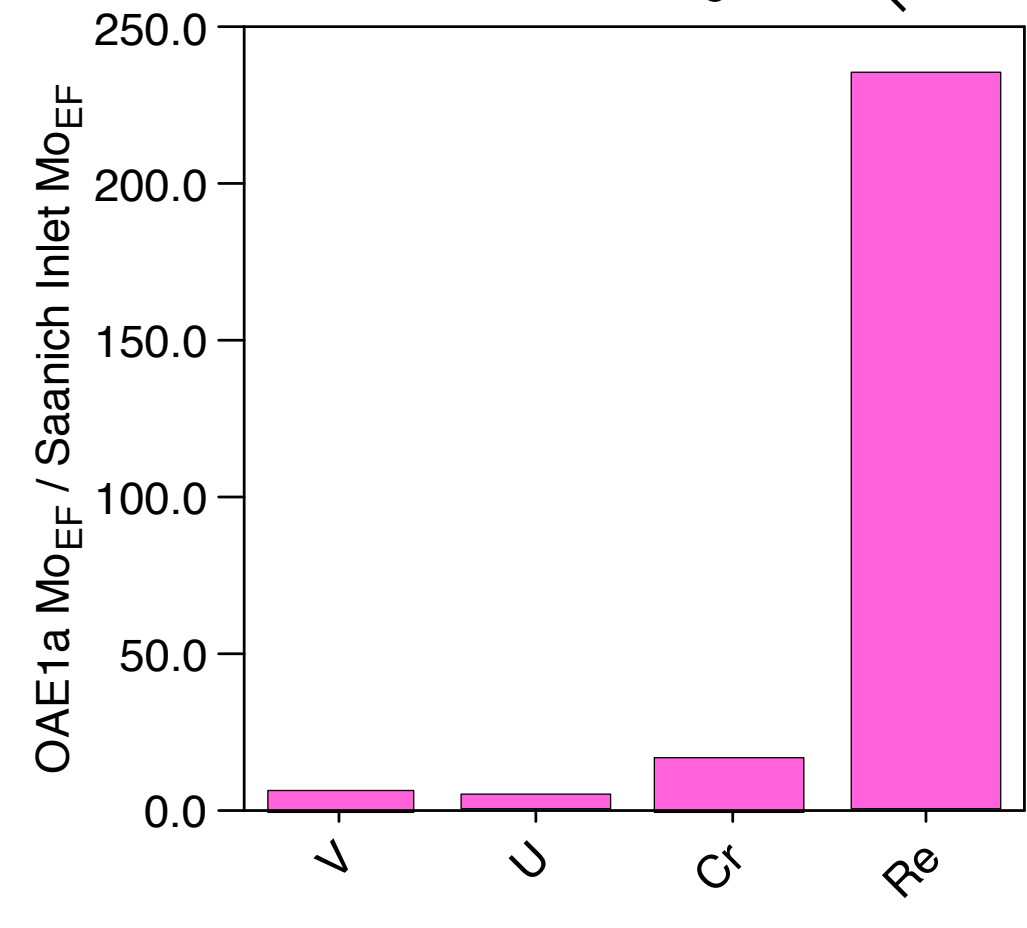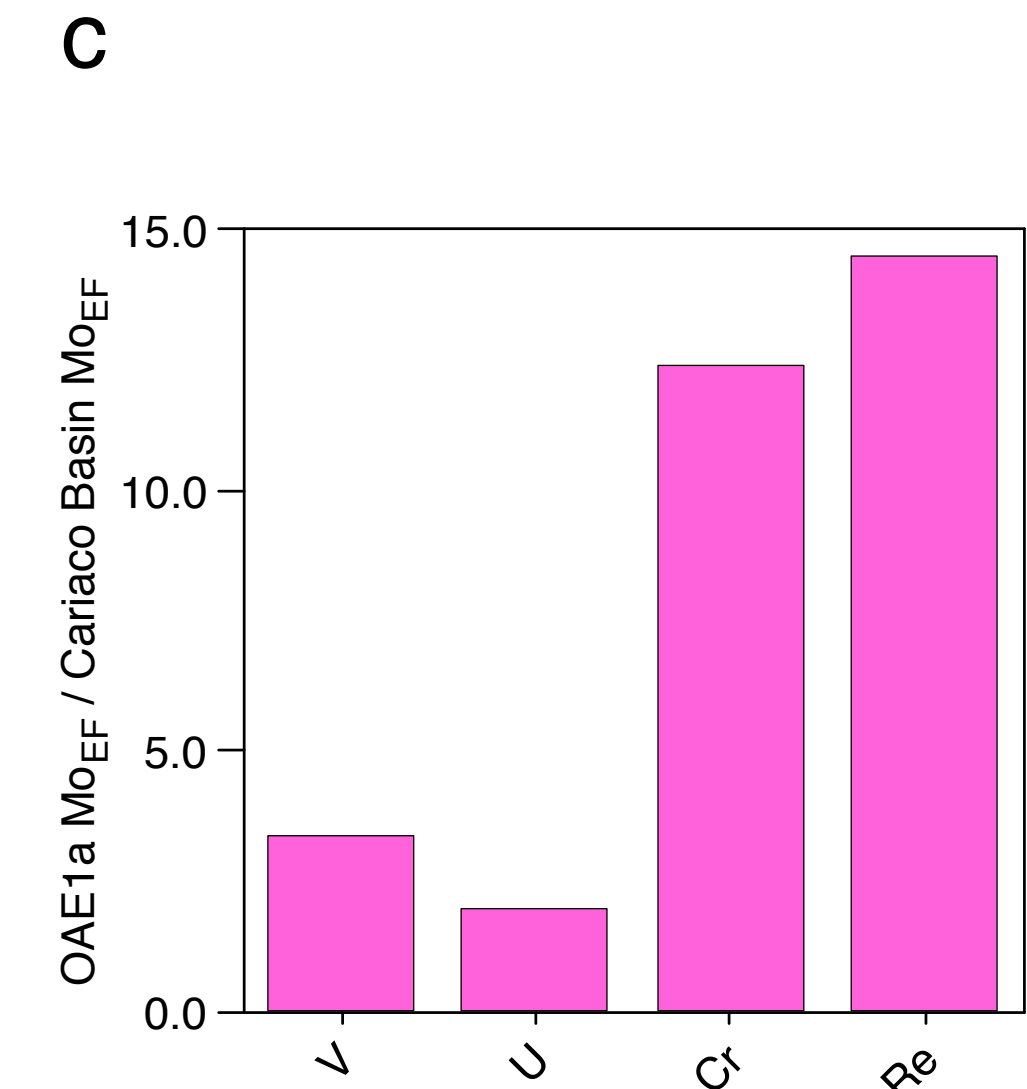540 *the United States of America* 2016, **113**(41)**:** 11447-11452.

541

542 25. Erba E, Bottini C, Weissert HJ, Keller CE. Calcareous Nannoplankton
543 Response to Surface-Water Acidification Around Oceanic Anoxic Event 1a.
544 *Science* 2010, **329**(5990)**:** 428-432.

545

546 26. Malinverno A, Erba E, Herbert TD. Orbital tuning as an inverse problem:
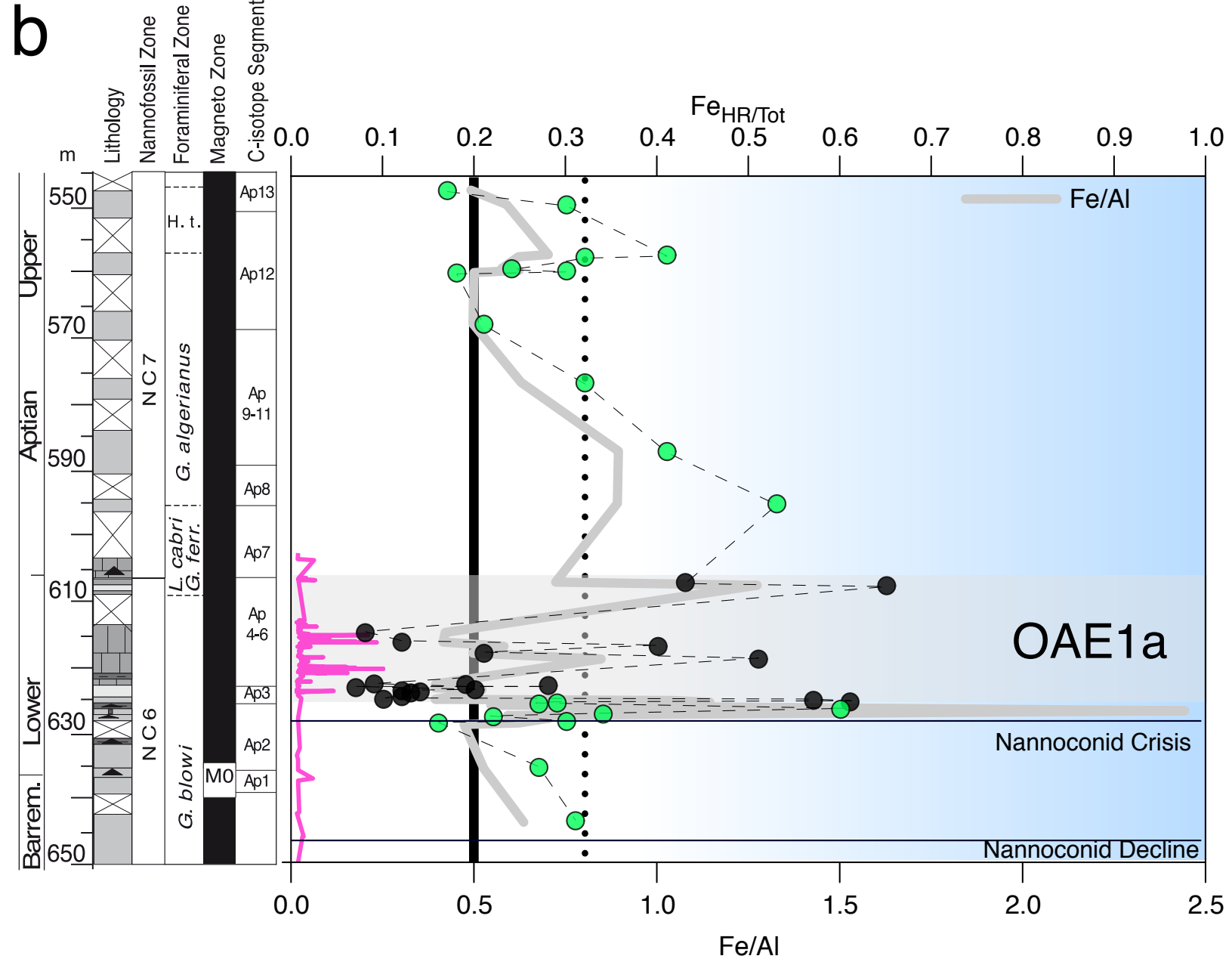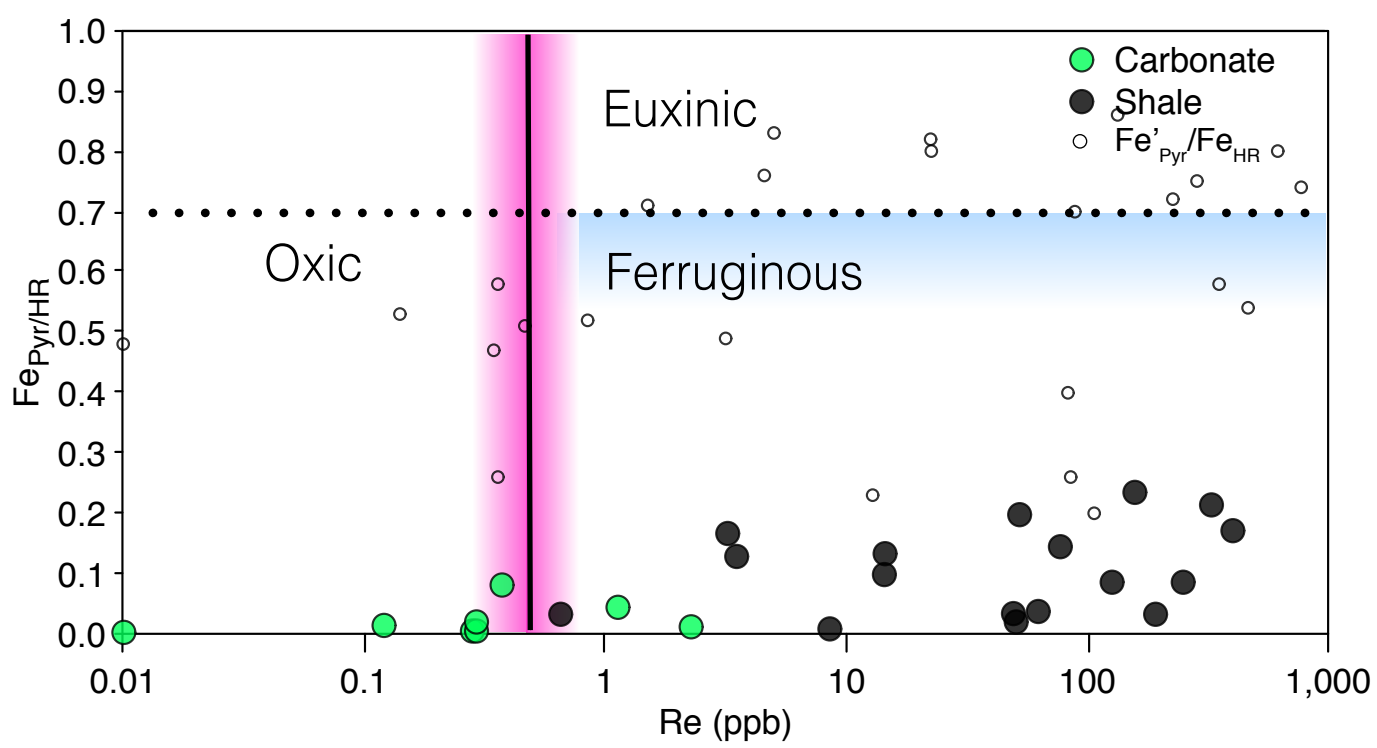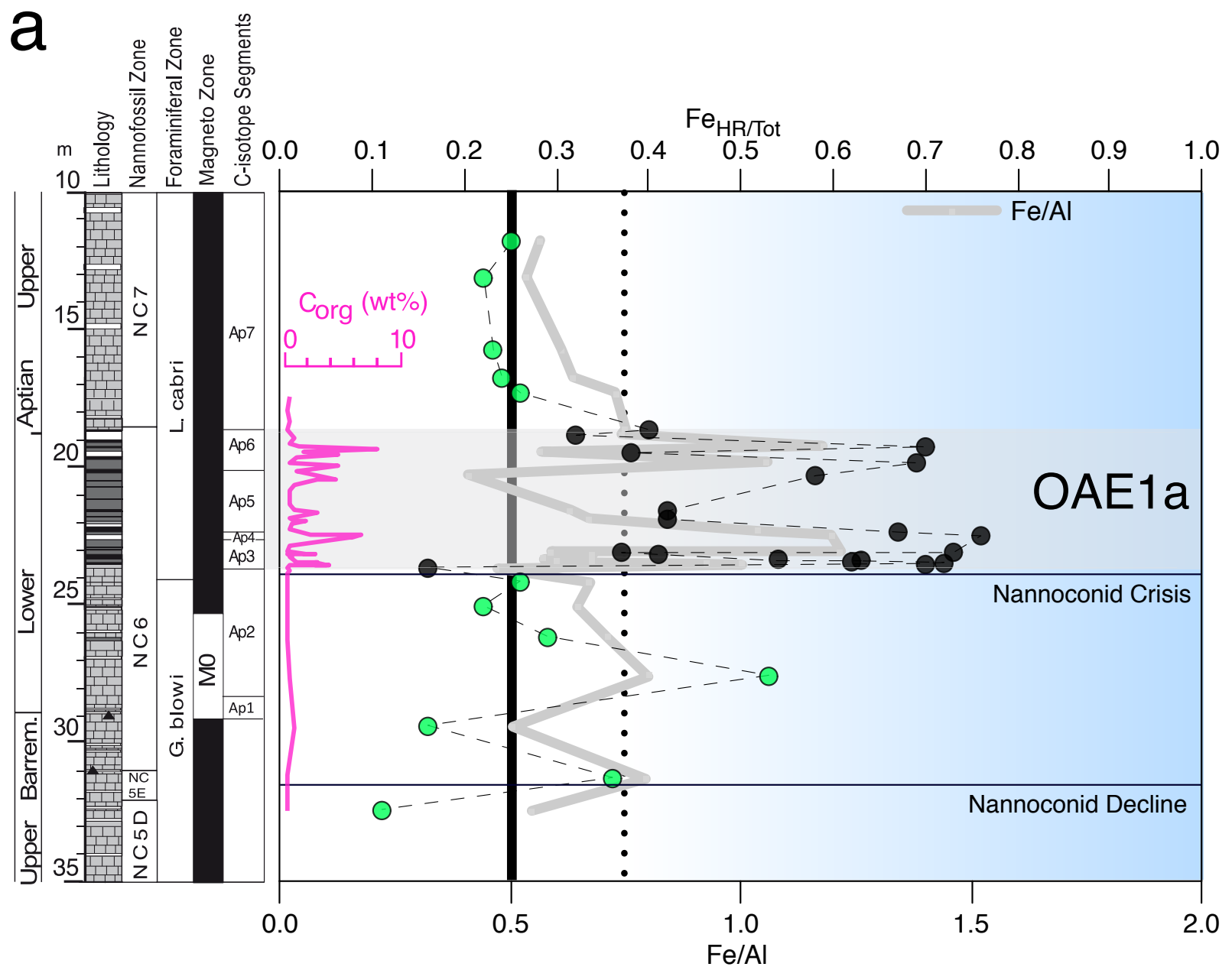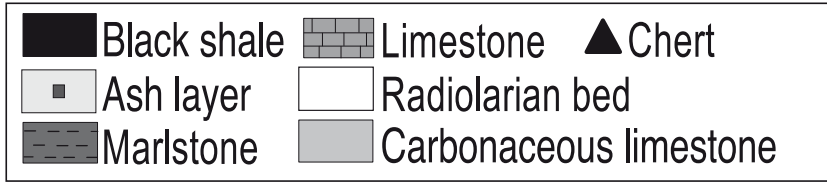547 Chronology of the early Aptian oceanic anoxic event 1a (Selli Level) in the
548 Cismon APTICORE. *Paleoceanography* 2010, **25**.

549

550 27. Lyons TW, Severmann S. A critical look at iron paleoredox proxies: New
551 insights from modern euxinic marine basins. *Geochimica Et Cosmochimica*
552 *Acta* 2006, **70**(23)**:** 5698-5722.

553

554 28. Canfield DE, Raiswell R, Bottrell S. The reactivity of sedimentary iron
555 minerals toward sulfide. *American Journal of Science* 1992, **292**(9)**:** 659-683.

556

557 29. Poulton SW, Canfield DE. Development of a sequential extraction procedure
558 for iron: implications for iron partitioning in continentally derived
559 particulates. *Chemical Geology* 2005, **214**(3-4)**:** 209-221.

560

561 30. Canfield DE, Thamdrup B, Hansen JW. The anaerobic degradation of organic
562 matter in Danish coastal sediments: iron reduction, manganese reduction,
563 and sulfate reduction. *Geochimica Et Cosmochimica Acta* 1993, **57**(16)**:** 3867-
564 3883.

565

566 31. Clarkson MO, Poulton SW, Guilbaud R, Wood RA. Assessing the utility of
567 Fe/Al and Fe-speciation to record water column redox conditions in
568 carbonate-rich sediments. *Chemical Geology* 2014, **382:** 111-122.

569

570 32. Poulton SW, Fralick PW, Canfield DE. The transition to a sulphidic ocean
571 similar to 1.84 billion years ago. *Nature* 2004, **431**(7005)**:** 173-177.

572

573 33. Calvert SE, Pedersen TF. Geochemistry of recent oxic and anoxic marine
574 sediments: implications for the geological record. *Mar Geol* 1993, **113**(1-2)**:**
575 67-88.

576

577 34. Tribovillard N, Algeo TJ, Lyons T, Riboulleau A. Trace metals as paleoredox
578 and paleoproductivity proxies: An update. *Chemical Geology* 2006, **232**(1-2)**:**
579 12-32.

580

581 35. McLennan SM. Relationships between the trace element composition of
582 sedimentary rocks and upper continental crust. *Geochemistry Geophysics*
583 *Geosystems* 2001, **2:** art. no.-2000GC000109.

584

585 36. Westermann S, Stein M, Matera V, Fiet N, Fleitmann D, Adatte T*, et al.* Rapid
586 changes in the redox conditions of the western Tethys Ocean during the early
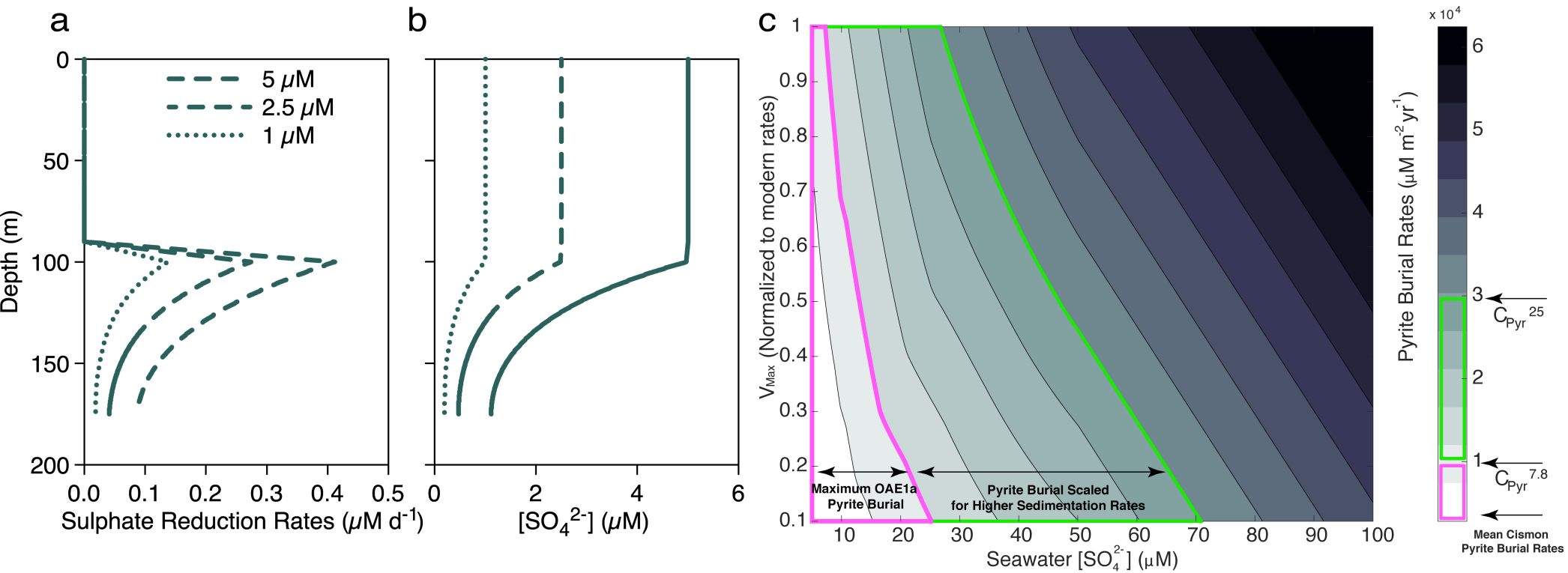
587   Aptian oceanic anoxic event. *Geochimica Et Cosmochimica Acta* 2013, **121:**
588   467-486.
589

590   37.   Follmi KB. Early Cretaceous life, climate and anoxia. *Cretaceous Research*
591   2012, **35:** 230-257.
592

593   38.   Hardisty DS, Lyons TW, Riedinger N, Isson TT, Owens JD, Aller RC*, et al.* An
594   evaluation of sedimentary molybdenum and iron as proxies for pore fluid
595   paleoredox conditions. *American Journal of Science* 2018, **318**(5)**:** 527-556.
596

597   39.   Bertine KK, Turekian KK. Molybdenum in marine deposits. *Geochimica et*
598   *Cosmochimica Acta* 1973, **37**(6)**:** 1415-1434.
599

600   40.   Slotznick SP, Eiler JM, Fischer WW. The effects of metamorphism on iron
601   mineralogy and the iron speciation redox proxy. *Geochimica Et Cosmochimica*
602   *Acta* 2018, **224:** 96-115.
603

604   41.   Kraal P, Slomp CP, Forster A, Kuypers MMM, Sluijs A. Pyrite oxidation during
605   sample storage determines phosphorus fractionation in carbonate-poor
606   anoxic sediments. *Geochimica Et Cosmochimica Acta* 2009, **73**(11)**:** 3277-
607   3290.
608

609   42.   Crowe SA, Maresca JA, Jones C, Sturm A, Henny C, Fowle DA*, et al.* Deep-water
610   anoxygenic photosythesis in a ferruginous chemocline. *Geobiology* 2014,
611   **12**(4)**:** 322-339.
612

613   43.   Canfield DE, Stewart FJ, Thamdrup B, De Brabandere L, Dalsgaard T, Delong
614   EF*, et al.* A Cryptic Sulfur Cycle in Oxygen-Minimum-Zone Waters off the
615   Chilean Coast. *Science* 2010, **330**(6009)**:** 1375-1378.
616

617   44.   Habicht KS, Canfield DE. Sulfur isotope fractionation during bacterial sulfate
618   reduction in organic-rich sediments. *Geochimica Et Cosmochimica Acta* 1997,
619   **61**(24)**:** 5351-5361.
620

621   45.   Kunzmann M, Bui TH, Crockford PW, Halverson GP, Scott C, Lyons TW*, et al.*
622   Bacterial sulfur disproportionation constrains timing of Neoproterozoic
623   oxygenation. *Geology* 2017, **45**(3)**:** 207-210.
624

625   46.   Blattler CL, Jenkyns HC, Reynard LM, Henderson GM. Significant increases in
626   global weathering during Oceanic Anoxic Events 1a and 2 indicated by
627   calcium isotopes. *Earth and Planetary Science Letters* 2011, **309**(1-2)**:** 77-88.
628

629   47.   Calvert SE, Karlin RE. Relationships between sulphur, organic carbon, and
630   iron in the modern sediments of the Black Sea. *Geochimica Et Cosmochimica*
631   *Acta* 1991, **55**(9)**:** 2483-2490.
632

633 48. Martin JH, Knauer GA, Karl DM, Broenkow WW. VERTEX: carbon cycling in
634   the northeast Pacific. *Deep Sea Research Part A Oceanographic Research*
635   *Papers* 1987, **34**(2)**:** 267-285.

637 49. Böning P. Trace element signatures of Peruvian and Chilean upwelling
638   sediments. Universität Oldenburg, 2005.

640 50. Scholz F, Severmann S, McManus J, Noffke A, Lomnitz U, Hensen C. On the
641   isotope composition of reactive iron in marine sediments: Redox shuttle
642   versus early diagenesis. *Chemical Geology* 2014, **389:** 48-59.

644 51. Horner TJ, Pryer HV, Nielsen SG, Crockford PW, Gauglitz JM, Wing BA, *et al.*
645   Pelagic barite precipitation at micromolar ambient sulfate. *Nature*
646   *Communications* 2017, **8**.

648 52. Paris G, Adkins JF, Sessions AL, Webb SM, Fischer WW. Neoarchean
649   carbonate-associated sulfate records positive Delta S-33 anomalies. *Science*
650   2014, **346**(6210)**:** 739-741.

652 53. Mitchell MJ, Landers DH, Brodowski DF, Lawrence GB, David MB. Organic and
653   inorganic sulfur constituents of the sediments in three New York lakes: Effect
654   of site, sediment depth and season. *Water Air and Soil Pollution* 1984, **21**(1-
655   4)**:** 231-245.

657 54. Urban NR. Retention of sulfur in lake sediments. *Environmental Chemistry of*
658   *Lakes and Reservoirs* 1994, **237:** 323-369.

660 55. Fagerbakke KM, Heldal M, Norland S. Content of carbon, nitrogen, oxygen,
661   sulfur and phosphorus in native aquatic and cultured bacteria. *Aquatic*
662   *Microbial Ecology* 1996, **10**(1)**:** 15-27.

664 56. Kaplan IR, Emery KO, Rittenberg SC. The distribution and isotopic abundance
665   of sulphur in recent marine sediments off southern California. *Geochimica Et*
666   *Cosmochimica Acta* 1963, **27**(APR)**:** 297-&.

668 57. Chen CTA, Lin CM, Huang BT, Chang LF. Stoichiometry of carbon, hydrogen,
669   nitrogen, sulfur and oxygen in the particulate matter of the western North
670   Pacific marginal seas. *Marine Chemistry* 1996, **54**(1-2)**:** 179-190.

672 58. Raven MR, Fike DA, Gomes ML, Webb SM, Bradley AS, McClelland HLO.
673   Organic carbon burial during OAE2 driven by changes in the locus of organic
674   matter sulfurization. *Nature Communications* 2018, **9**.

676 59. Bottini C, Cohen AS, Erba E, Jenkyns HC, Coe AL. Osmium-isotope evidence
677   for volcanism, weathering, and ocean mixing during the early Aptian OAE 1a.
678   *Geology* 2012, **40**(7)**:** 583-586.

679

680   60.   Kaplan IR, Rittenberg SC. Microbiological fractionation of sulphur isotopes.
681   *Journal of General Microbiology* 1964, **34**(2)**:** 195-&.
682

683   61.   Utne-Palm AC, Salvanes AGV, Currie B, Kaartvedt S, Nilsson GE, Braithwaite
684   VA*, et al.* Trophic Structure and Community Stability in an Overfished
685   Ecosystem. *Science* 2010, **329**(5989)**:** 333-336.
686

687   62.   Damste JSS, Wakeham SG, Kohnen MEL, Hayes JM, Deleeuw JW. A 6,000–year
688   sedimentary molecular record of chemocline excursions in the Black Sea.
689   *Nature* 1993, **362**(6423)**:** 827-829.
690

691   63.   van Breugel Y, Schouten S, Tsikos H, Erba E, Price GD, Damste JSS.
692   Synchronous negative carbon isotope shifts in marine and terrestrial
693   biomarkers at the onset of the early Aptian oceanic anoxic event 1a: Evidence
694   for the release of C-13-depleted carbon into the atmosphere.
695   *Paleoceanography* 2007, **22**(1).
696

697   64.   Canfield DE, Teske A. Late Proterozoic rise in atmospheric oxygen
698   concentration inferred from phylogenetic and sulphur-isotope studies.
699   *Nature* 1996, **382**(6587)**:** 127-132.
700

701   65.   Crowe SA, Jones C, Katsev S, Magen C, O'Neill AH, Sturm A*, et al.*
702   Photoferrotrophs thrive in an Archean Ocean analogue. *Proceedings of the*
703   *National Academy of Sciences of the United States of America* 2008, **105**(41)**:**
704   15938-15943.
705

706   66.   Bottini C, Erba E, Tiraboschi D, Jenkyns H, Schouten S, Sinninghe Damsté J.
707   Climate variability and ocean fertility during the Aptian Stage. *Climate of the*
708   *Past* 2015, **11**(3)**:** 383-402.
709

710   67.   Menegatti AP, Weissert H, Brown RS, Tyson RV, Farrimond P, Strasser A*, et al.*
711   High-resolution delta C-13 stratigraphy through the early Aptian "Livello
712   Selli" of the Alpine Tethys. *Paleoceanography* 1998, **13**(5).
713

714   68.   Li Y-X, Bralower TJ, Montañez IP, Osleger DA, Arthur MA, Bice DM*, et al.*
715   Toward an orbital chronology for the early Aptian oceanic anoxic event
716   (OAE1a,~ 120 Ma). *Earth and Planetary Science Letters* 2008, **271**(1)**:** 88-
717   100.
718

719   69.   Li Y, Schoonmaker J. *Chemical composition and mineralogy of marine*
720   *sediments*, vol. 7. na, 2003.
721

722   70.   Paytan A, Kastner M, Campbell D, Thiemens MH. Seawater sulfur isotope
723   fluctuations in the cretaceous. *Science* 2004, **304**(5677)**:** 1663-1665.
724

Black shale	Limestone	▲ Chert
Ash layer	Radiolarian bed	
Marlstone	Carbonaceous limestone	
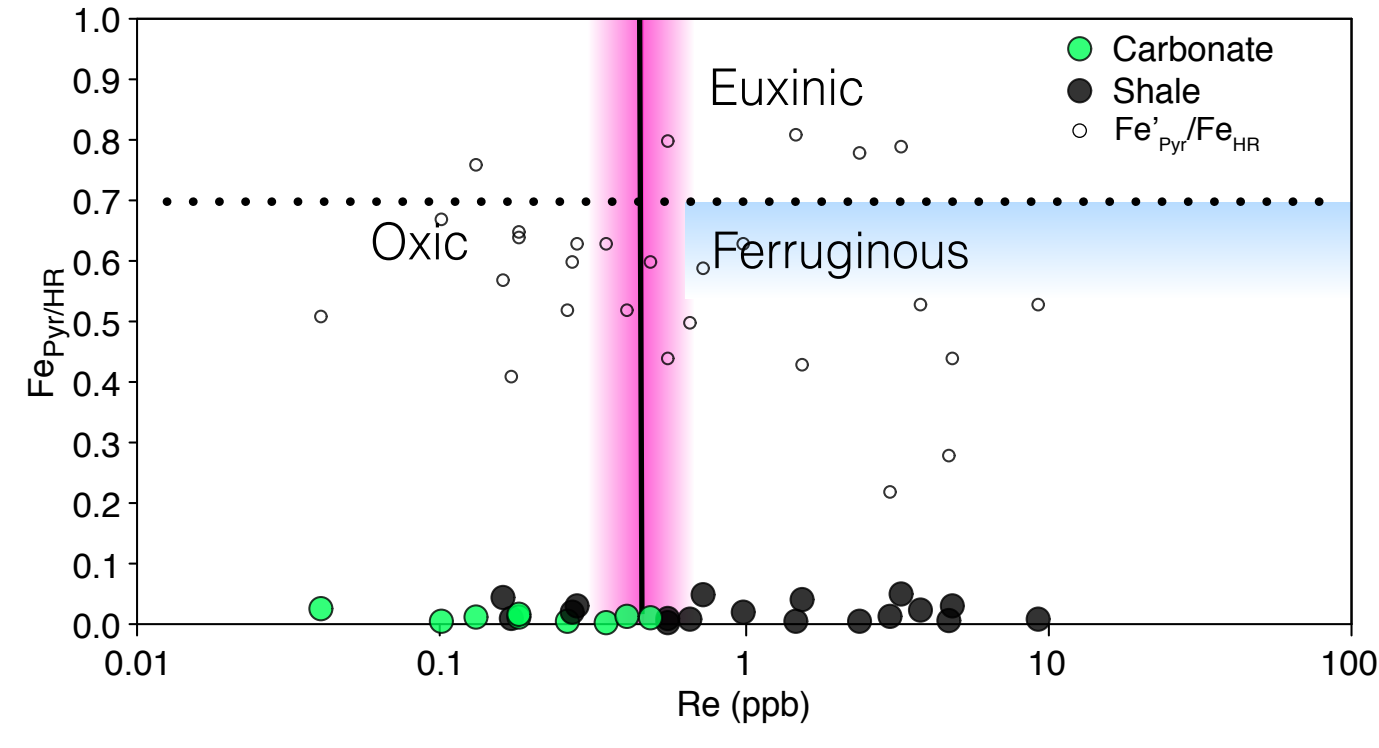
Ocean Fertilization and Enhanced Primary Productivity

Pyrite Burial

Ontong Java Eruption   **Caribbean LIP**

Evaporite Burial   **?**